Supplemental Information for "Seismic characterization of the subsurface and anthropogenic noise at the LUNA Moon analog facility"

Brigitte Knapmeyer-Endrun[1], Martin Knapmeyer[2], Olav Cornelius[3], Hans-Herbert Fischer[4], Maria Hallinger[1], Cinzia Fantinati[1], Oliver Küchemann[1], Michael Maibaum[1]

[1] *Microgravity User Support Center, German Aerospace Center (DLR), Cologne, Germany*

[2] *Institute for Planetary Research, German Aerospace Center (DLR), Berlin, Germany*

[3] *Department of Earth and Planetary Sciences, Institute of Geophysics, ETH Zurich, Zurich, Switzerland*

[4] *retired, formerly at: Microgravity User Support Center, German Aerospace Center (DLR), Cologne, Germany*

Contents of this file

S1 Details on data sets and methods of analysis

S1.1 Refraction profile

The seismic refraction profile used 24 vertical-component 10 Hz geophones deployed over 46 meters length, with a geophone spacing of 2 m, except for the first two geophones next to the shot-points at the ends of the line that were placed 1 m apart. A 10 kg hammer was used as a source. A trigger geophone near the source started the data recording. Shot points were located at 0 m, 15 m, 25 m, 35 m and 46 m along the profile, respectively (Supplemental Fig. S1). Locations of geophones and shot points along the profile were determined with a measurement tape. At each shot point, signals from 5 hammer blows were stacked after first assuring a good signal-to-noise ratio for each individual shot. The geophones were recording at 40 kHz for 8192 samples (i.e. 204.8 ms), with 5 ms pre-trigger time to allow for confident picking of the first onset also at close distances to the shot. In addition, data from one shot point at a larger offset from the profile, at 52.9 m, was recorded at 1 kHz for a duration of 4.096 s and without pre-trigger for use in multi-channel analysis of surface waves (MASW, Supplemental Fig. S1c). This specific distance was chosen due to practical constraints by the road.

The geophone recordings of shots at the five points between 0 and 46 m profile length were used for a P-wave refraction seismic analysis. The first onset on all traces was picked, including uncertainties.

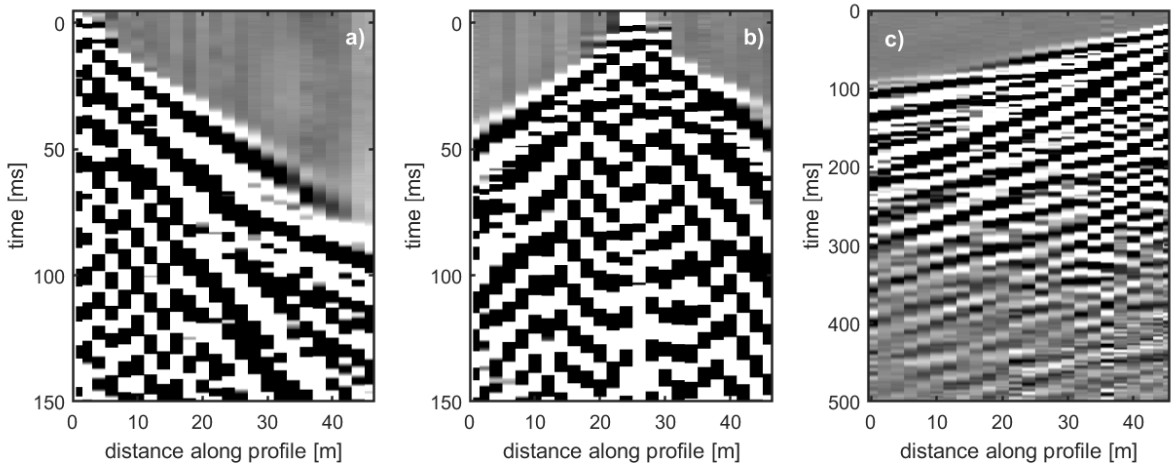

Supplemental Figure S1: Shot recordings along seismic line, showing hammer shots at (a) 0 m, (b) 25 m used for refraction seismic analysis, and (c) 52.9 m used for MASW analysis.

For more distant traces (especially at offsets larger than 25-30 m from the shot), the data were filtered with a zero-phase Butterworth bandpass of order 7 between 0.5 and 500 Hz to reduce both very high-frequency and long-period noise. Unfiltered and filtered traces were considered simultaneously in these cases to ensure consistent picking. Since no clear differences between the travel time for various shot positions were apparent, and few data points were available for the deepest layer, data from all shots were combined in a single travel-time vs. offset plot for interpretation (Supplemental Fig. S2).

MASWaves (Olafsdottir et al., 2018) was applied across a frequency range of 2 to 60 Hz at 1 Hz intervals and a velocity range of 100 to 600 m/s at 1 m/s intervals along the geophone profile. The resulting curve shows nearly constant phase velocities between 270 m/s and 310 m/s, which are best defined between 9 Hz and 26 Hz (Supplemental Fig. S3).

S1.2 Seismic array

The seismometer array, designed for repeated reference measurements at specific times during LUNA construction, consisted of four short-period three-component Lennartz Le-3Dlite seismometers (eigenfrequency 1 Hz), deployed in a triangle around a central station, where the radius of the circle through the three corners of the triangle was 8 m. Thus, while the lay-out principle is the same as for Apollo 17's LSPE, the aperture of our array is significantly smaller to allow for a 1:1 repetition of the measurements within the completed LUNA building. The central station was enhanced by placing a Nanometrics Trillium compact 120 s broad-band seismometer next to the Lennartz sensor. All sensors were installed in shallow holes in the soil on leveled concrete tiles and covered in soil. Relative locations of the stations were determined by triangulation with a tape measure and a laser distance measurement system, and orientation of the stations was determined with a compass. Based on the measured relative distances between all station pairs, least squares solutions for sensor locations were determined, including two

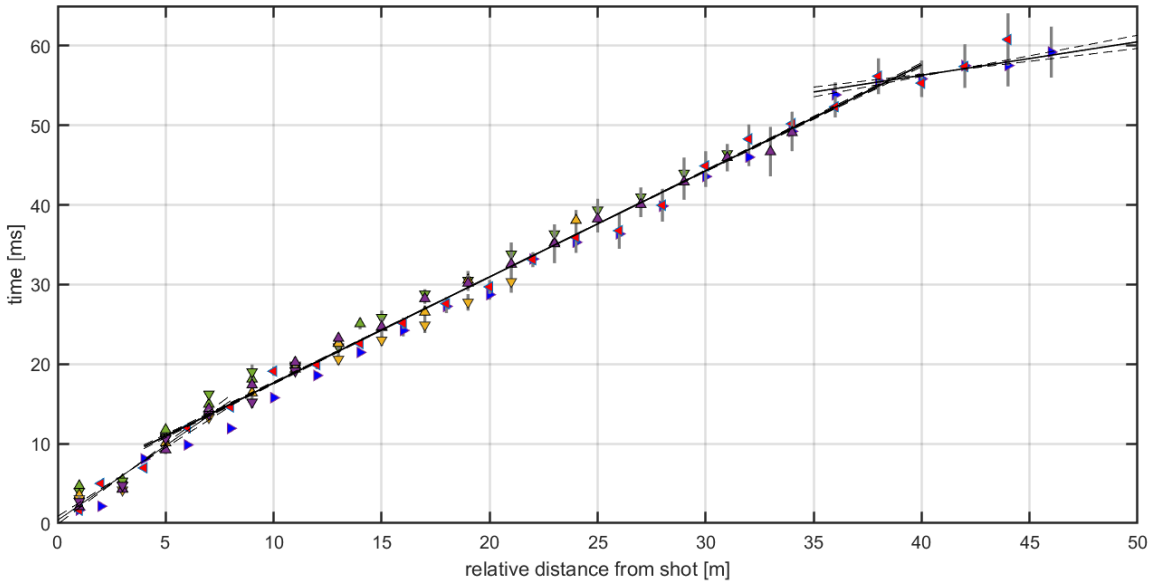

Supplemental Figure S2: Travel times vs. offset for the reflection seismic profiles. Different colors of triangles indicate different shots, where triangles of the same color pointing in opposite directions relate to data points to the north and south of the shot point. Vertical gray bars give uncertainties in the travel time picks. Solid black lines are least-squares fits to the data points, with dashed black lines indicating uncertainty from boot-strapping over 10,000 realizations.

markers provided by the constructing company that represented the locations of the South-East and South-West corners of the future building. Data of all seismometers were recorded with 200 Hz sampling rate. Recordings started on a Thursday afternoon and continued to Sunday afternoon, though about 13 hours of data of the short-period station on the north-western corner of the triangle were lost as it got dug up and knocked over by an animal, probably a badger, during Saturday night.

Data from the array were analysed using high-resolution three-component Rayleigh beam forming (RTBF, Wathelet et al., 2018), as implemented in Geopsy (Wathelet et al., 2020), as well as conventional (Lacoss et al., 1969) and high-resolution beam-forming (Capon, 1969). We compared dispersion results for data from several low-noise time windows on different days to ensure we invert a curve with stable features. Results across different time windows were consistent (e.g. Endrun et al., 2010), and for our final curves, we focused on data recorded during midnight and 9 am UTC on Saturday, as these contain little contamination due to transient sources. Conventional frequency-wavenumber analysis provided the most noisy curves, with values at individual frequencies oscillating around an average curve. The curves from high-resolution beam-forming and RTBF are much smoother, and show good agreement. No clear higher mode signal was identified in the RTBF data. Considering horizontal components generally lent less clear signals, with no recognizable dispersion curves. The resulting vertical component dispersion curve shows good agreement with the MASW results within the frequency band covered by both, and extends to frequencies of about 5.5 Hz (Supplemental Fig. S3).

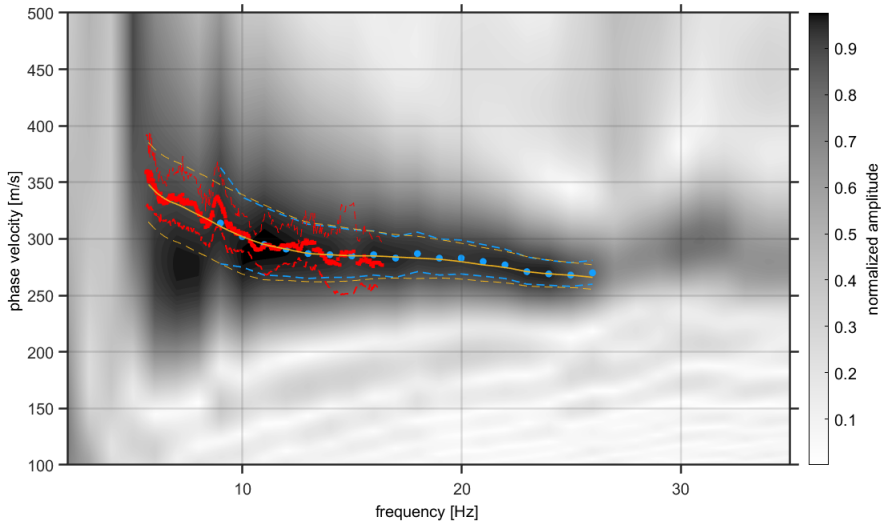

Supplemental Figure S3: Grayscale background indicates the dispersion image obtained by MASW. Blue dots with standard deviation show the corresponding fundamental mode dispersion curve, while red dots with standard deviation are the results of RTBF for the array. Orange curve with standard deviation outlines the smooth curve combining both constraints used as input to the inversion.

In addition to a Rayleigh wave dispersion curve estimate, RTBF also provides an array-derived estimate of the Rayleigh wave ellipticity, including the sense of rotation of the Rayleigh wave particle motion (Hobiger et al., 2012; Wathelet et al., 2018), over the same frequency band as the dispersion curve. This is expressed in terms of the signed ellipticity angle (Maranò et al., 2017), while single-station measurements only provide estimates of the absolute value. Negative angles point to retrograde particle motion, whereas positive angles indicate prograde particle motion. The peak and trough correspond to angles of 90^o and 0^o, respectively, and the relation between the ellipticity angle ϵ and the HVSR is given by

$$HVSR = |\tan \epsilon| \tag{1}$$

Using the same time window as for the dispersion analysis, three-component spatial autocorrelation functions (SPAC Aki, 1957; Köhler et al., 2007) were calculated for two sets of interstation distances, with radii of 7 to 9 m and 13 to 15 m, respectively. Although the raw data, indicated by dots with error bars at individual frequencies in Supplemental Fig. S4, show the typical Bessel-function shapes, the scatter between adjacent data points get higher at high frequencies, especially for the larger distance. This could be due to less clear signals at higher frequencies for larger inter-station spacing, lateral variations in small-scale structure across the spatial scale considered here, or the generally higher noise level at frequencies above 10 Hz (Fig. 3). Besides, the vertical curves show a deviation from the value of 1 expected at low frequencies at frequencies below 1 Hz. Accordingly, we cut the curves to leave out those values and the data most affected by noise at high frequencies, and use smoothened versions of the curves

in the inversion (bold lines in Supplemental Fig. S4).

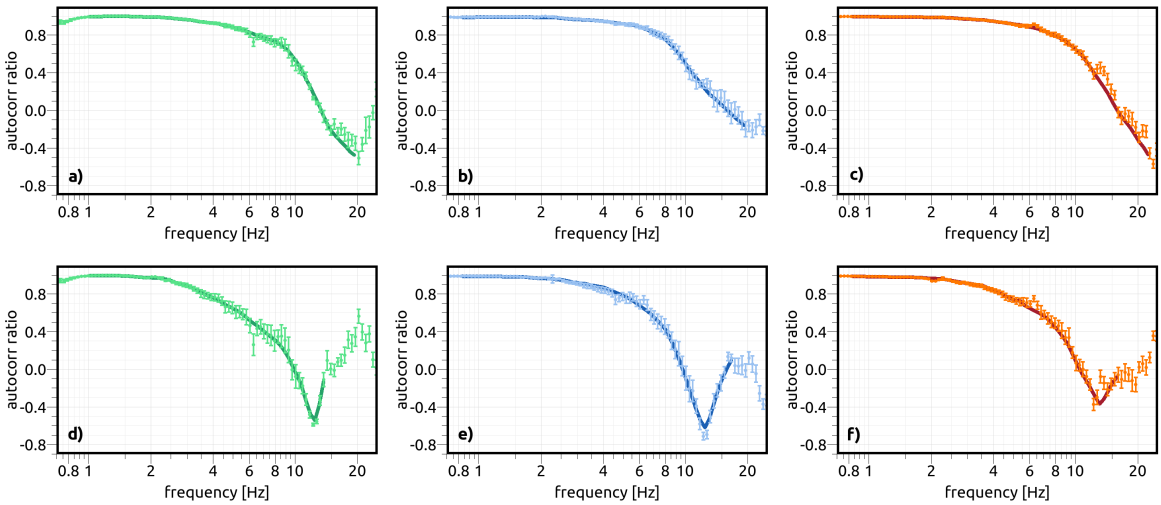

Supplemental Figure S4: Spatial autocorrelation curves, showing smoothed versions used as input to the inversion (thick solid curves) as well as measured raw data (thinner, lighter-colored lines give error bars). a) to c) are for interstation distances of 7 to 9 m, and d) to f) are for larger interstation distances with a radius of 13 to 15 m. a) and d) shows vertical components, b) and e) radial components, and c) and f) transverse components.

In addition, H/V spectral ratios (HVSR Nakamura, 1989; Bonnefoy-Claudet et al., 2006) were computed over 6 hours of data, using time windows of 80 times the given period with 5% overlap, with spectral smoothing according to Konno and Ohmachi (1998). Those are compared to Rayleigh wave ellipticity curves derived using RayDec (Hobiger et al., 2009) for the same time window, for which results from 36 calculations covering 10 min each were averaged. HVSR curves were derived from the array measurements at the LUNA location and from the long-term installation in the Microgravity User Support Center (MUSC) building (Supplementary Fig. S5).

The HVSR curves from the array show a broad agreement over different time windows and over all four sensor locations, with a distinct maximum at 0.76 Hz. For the comparison with RayDec, a time window from 00:00 to 06:00 UTC on a Saturday was chosen, to select data that are relatively free of large transient signals due to traffic. The RayDec results that are based on identifying time windows that dominantly contain Rayleigh waves have the same peak frequency, but in general lower amplitudes than the H/V curve, as expected when contributions from e.g. Love waves are removed. The RayDec algorithm also does not apply any smoothing, so the resulting curves look a bit more rough. H/V spectral ratios derived from the long-term installation in the MUSC building consistently show a spectral peak at 0.68 Hz, though maximum amplitude and exact shape of the H/V curve differ somewhat over time, as has previously been observed related to variable noise sources (e.g Endrun et al., 2010). The H/V peak frequency is also consistent with the RayDec results, which were again calculated for a time window from

00:00 to 06:00 UTC on a Saturday.

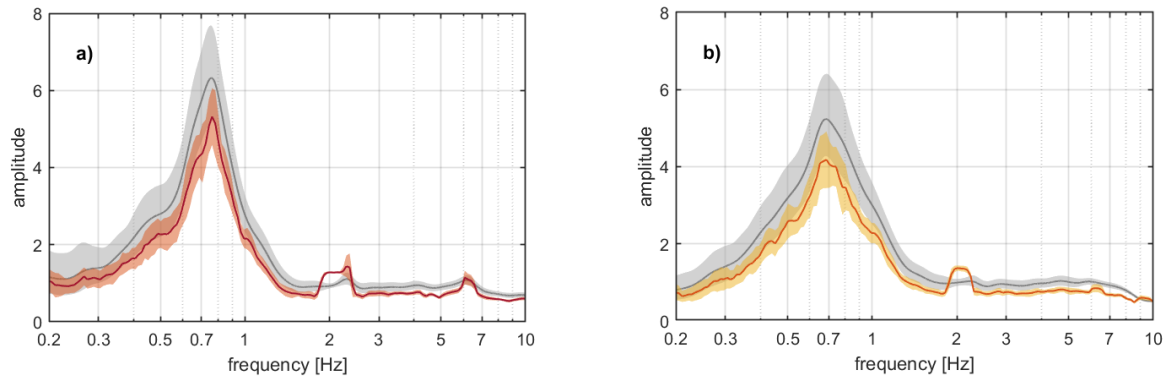

Supplemental Figure S5: H/V spectral ratios (gray) with standard deviations and Rayleigh wave ellipticity (colored) derived by RayDec with standard deviations calculated over 6 hours of data (00:00-06:00 UTC) on a Saturday. a) Central station of the four-element array at the LUNA location (broad-band seismometer) b) Broad-band station in the MUSC building.

Both RayDec-derived curves show additional maxima around 2 Hz, and around 6.25 Hz in the case of the measurement at the LUNA location, that are related to spectral peaks likely associated with anthropogenic sources, and not related to subsurface structure. Considering the resolution in measuring the peak frequency and the availability of only two data points, the evidence for a spatial trend in H/V peaks is not strong and should in the future be bolstered by more measurement across the whole campus. Still, the data hint at a slight decrease in peak frequency towards the west, with the value obtained in the MUSC building closer to that previously measured at a location about 1 km west of LUNA, i.e. 0.6 to 0.67 Hz (Parolai et al., 2004). This trend is in keeping with the large-scale south-westerly dip direction of the sediment-bedrock interface (Tyagunov et al., 2006). Accordingly, the bedrock depth below LUNA is expected to be less than the 200 m that were derived as a minimum estimate for the location on the western DLR campus by Parolai et al. (2004).

S1.3 Long-term test recording

The Trillium compact 120 s seismometer was installed on the concrete floor (below the actual floor tiles in the space available for cable routing) of an unused room on the ground floor in the annex to the building housing the MUSC, which does not have a cellar. As the location of the seismometer was close to the outer wall of the building, the concrete floor is however not directly located on the natural soil, but some thermal insulation in the form of rigid foam slabs is sandwiched in-between. The sensor was covered by a weighted plastic bucket to provide shielding against air movements, and the seismometer was oriented parallel to one of the walls of the building that strikes North-South. Data were continuously recorded at 200 Hz sampling rate and streamed to an internal seedlink server, and timing information provided via NTP.

For the PPSD shown in Fig. 3a), we combined data from June, 21st 2023 to August, 10th 2023 and from December, 21st 2023 to April, 22nd 2024, whereas in Supplemental Figure S6, we show both time windows individually to better highlight differences between summer (Supplemental Fig. S6a) and winter time (Supplemental Fig. S6b) in the secondary microseisms, which, in Germany, are mainly generated by storms over the North Atlantic (Essen et al., 2003). PPSDs were calculated with ObsPy (The ObsPy Development Team, 2022), using the default settings of one hour window length with 50% overlap for the calculation of spectra, and frequency binning at 1/8 of an octave while smoothing by averaging PSDs over a full octave around every central frequency.

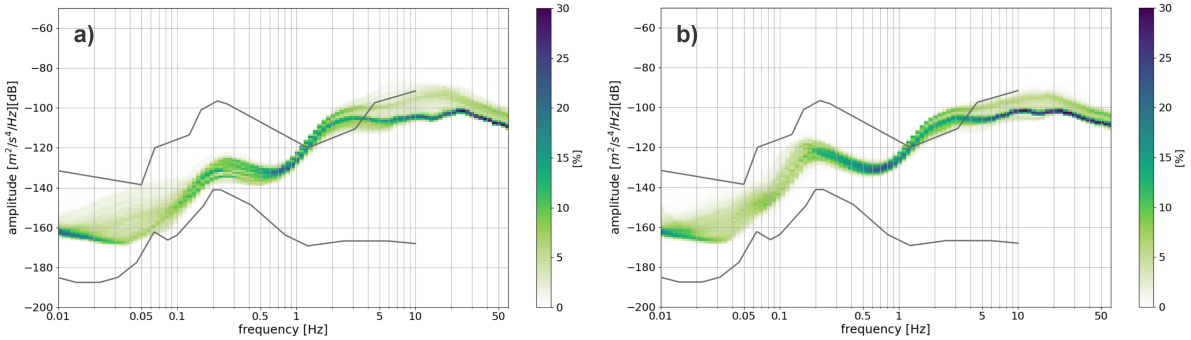

Supplemental Figure S6: (a) Vertical-component PPSD recorded in the MUSC building during summer, from June, 21st 2023 to August, 10th 2023. (b) Vertical-component PPSD recorded in the MUSC building during winter, from December, 21st 2023 to April, 22nd 2024.

When the broad-band sensor was needed for other tests, a Lennartz three-component Le-3Dlite sensor (eigenfrequency 1 Hz) was installed in the same place and in the same manner, except that no shielding from air motion was required for the short-period sensor. Data were likewise recorded at 200 Hz sampling rate and streamed via the seedlink protocol, with timing information via NTP.

S2 Earthquake recordings

To judge the quality of future seismic recordings with the permanent broad-band station in LUNA, we also checked seismograms of earthquakes recorded during the long-term test in the MUSC building. We show two examples here, for a teleseismic and a local event.

The teleseismic example (Fig. S8) is an event with M_W=6.6 offshore Antigua and Barbuda (20.063^{o}N 61.102^{o}W, 14 km depth) that occurred on July, 10th 2023. The epicentral distance to the broad-band sensor installed on the DLR campus was 61^o. At a similar epicentral distance, Bensberg Observatory of University of Cologne (Robel, 1959) is running a permanent station (BQ.BNS) that uses the same seismometer and digitizer, but is sampled at 100 Hz. The observatory is located on Devonian bedrock of the Rhenish Massif, and the seismometer is installed in the cellar on a pillar decoupled from the rest of the building. The distance between the two stations is approximately 13 km. We directly compare digital

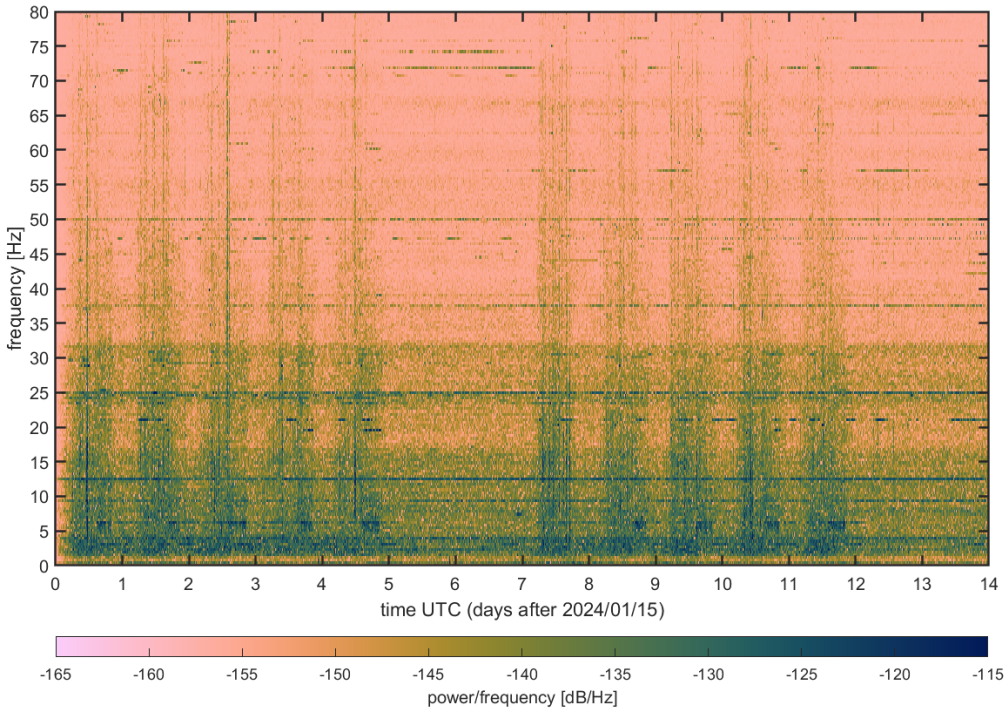

Supplemental Figure S7: Spectrogram of the vertical component seismic velocity data, registered with the broad-band instrument, for two weeks in January 2024. The time window covered (January, 15th to 29th) lies within the range where an elevated noise level in the 4 to 20 Hz frequency band was measured in the afternoon of most workdays (Fig. 4). Spectrograms demonstrate the concurrent occurrence of a signal with maximum energy around 5 to 6.5 Hz.

units, band-pass filtered between 1.25 and 200 s, here, as the two stations share the same hardware. All three components of the seismograms show a strong correspondence, at least up to 35 minutes after the first onset, well into the surface wave train (Fig. S8). A clear difference is however apparent within the P-wave onset and coda on the horizontal components, which show significantly higher amplitudes and also contain higher frequencies at our test installation, likely caused by reverberations in the thick sediments beneath the DLR site that are absent at BQ.BNS. As already indicated by the power spectral densities of the long-term installation (Fig. 3), it is expected that the broad-band seismometer in LUNA will be able to record significant teleseismic events at a quality comparable to stations of local networks.

An example of a local event recorded with the test installation is shown in Fig. S9. This seismogram was recorded with the short-period Lennartz sensor and is the smallest earthquake that was reliably identified in the data. It had a local magnitude of M_L=0.8 and occurred on October, 19th 2023 in Friesdorf, about 18 km away from the station, according to the catalog of Bensberg observatory (Universität zu Köln, 2023). Data were restituted to true ground velocity and filtered between 4 and 20 Hz, respectively. Though the noise level in this frequency range is apparent, specifically on the vertical component, P-

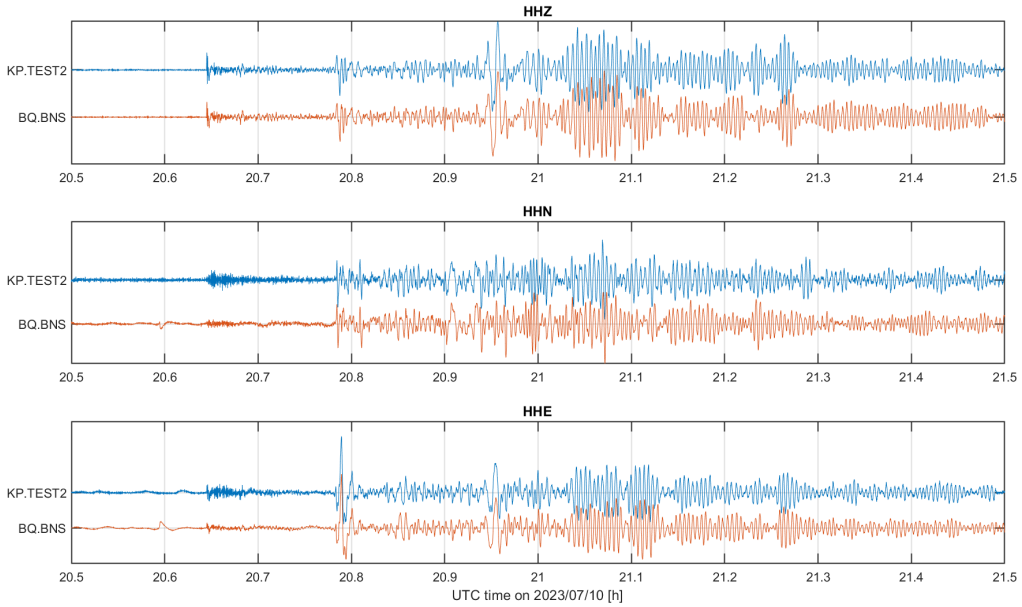

Supplemental Figure S8: Comparison of recordings of a teleseismic event in the Caribbean between the test installation (labeled KP.TEST2 here) and the permanent broad-band station at Bensberg observatory using the same hardware. Waveforms are in raw counts, band-pass filtered between 1.25 and 200 s.

and S-onset are clearly visible. The earthquake occurred around 07:36 pm UTC, translating to 09:36 pm local time, when human activity on the campus should be low. However, running machinery and air traffic were still contributing to the observed noise level.

While the Lower Rhine Embayment (LRE) is a region of moderate seismic activity, although coupled with a non-negligible level of risk (Pilz et al., 2020), the overwhelming fraction of earthquakes is small, with magnitudes below 2.0. The majority of recent seismic activity is also located either further to the west of Cologne along faults within the LRE, or further to the south, within the East Eifel region (e.g., Stammler et al., 2021). Still, during the test installation, we also recorded a few larger local events, with magnitudes up to 2.8. An earthquake of magnitude 2.3 was registered at 69 km distance during the night hours, whereas an earthquake with magnitude 1.9 at 45 km distance was also clearly visible during daytime on a weekday. While the comparatively low level of seismic activity combined with the noise conditions during daytime on weekdays means that any given future seismological use case in LUNA cannot rely on registering local seismicity during its test period, serendipitously recording local seismicity is still possible.

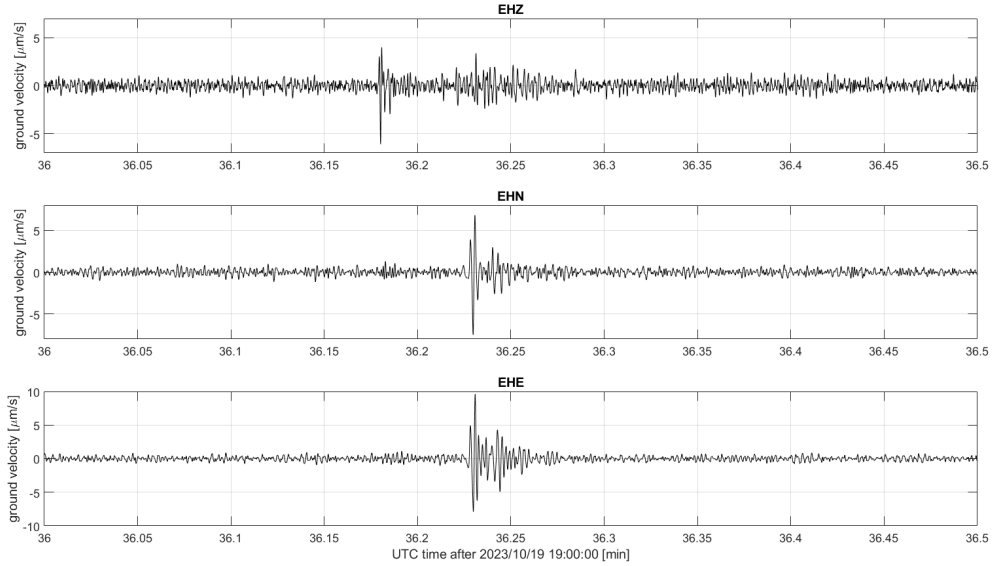

Supplemental Figure S9: Three-component recording of a local M_L=0.8 event near Friesdorf that occurred during the long-term test installation. Seismograms are band-pass filtered between 4 and 20 Hz.

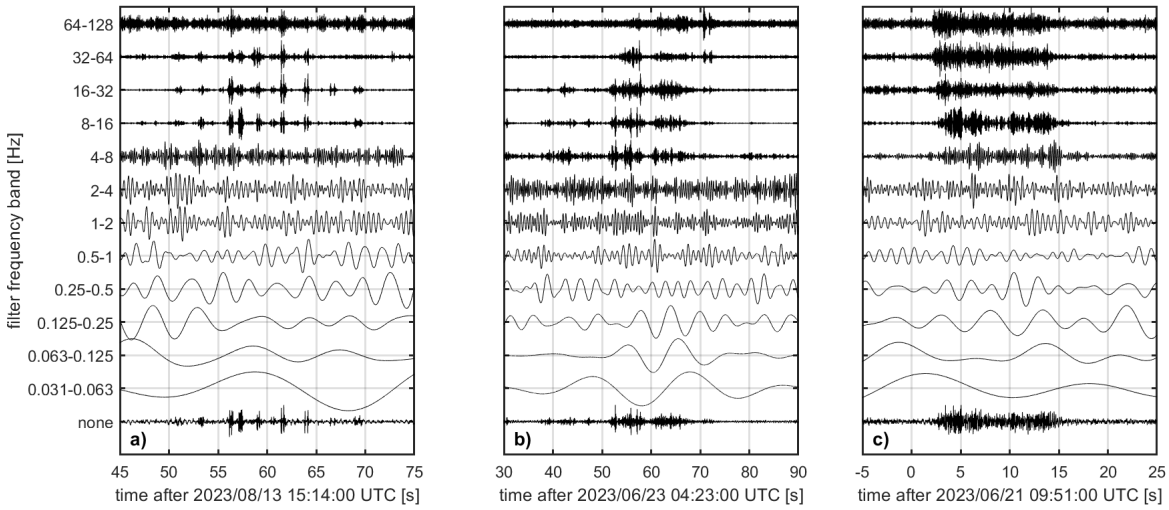

Supplemental Figure S10: Vertical component seismic velocity data, registered with the broad-band instrument, for three different transient sources, filtered within consecutive octave bands. a) Toyota Prius driving by the seismic array from west to east b) Bus passing by the long-term installation in the MUSC building from west to east c) Wind tunnel run, at about 220 m distance, recorded during the long-term installation in the MUSC building.

S3 Further information on on-site traffic

For Supplemental Fig. S11, the direction of travel of the car was assigned based on the distinctive signal pattern generated by the sequence of cracks and bumps in the road. The campus, and the road, end at the eastern margin of Fig. 1, with the road terminating near the entrance to the underground parking garage of the EAC. Hence, on the one full workday covered by array measurements, the amount of car traffic spikes in the morning between 8 and 9 am local time, when people arrive for work, and shows additional, broader maxima, between 12 and 2 pm local time (people heading for lunch and back) and 3 and 7 pm (people leaving for the weekend). Accordingly, the timing of cars driving west to east as identified here corresponds to time windows in the morning, or early afternoon, when people are arriving at EAC, whereas the timing of cars driving east to west corresponds to time windows around noon or in the afternoon when people are leaving EAC. During the weekend and during the nighttime, as expected, car traffic is low and mainly related to the on-site security service.

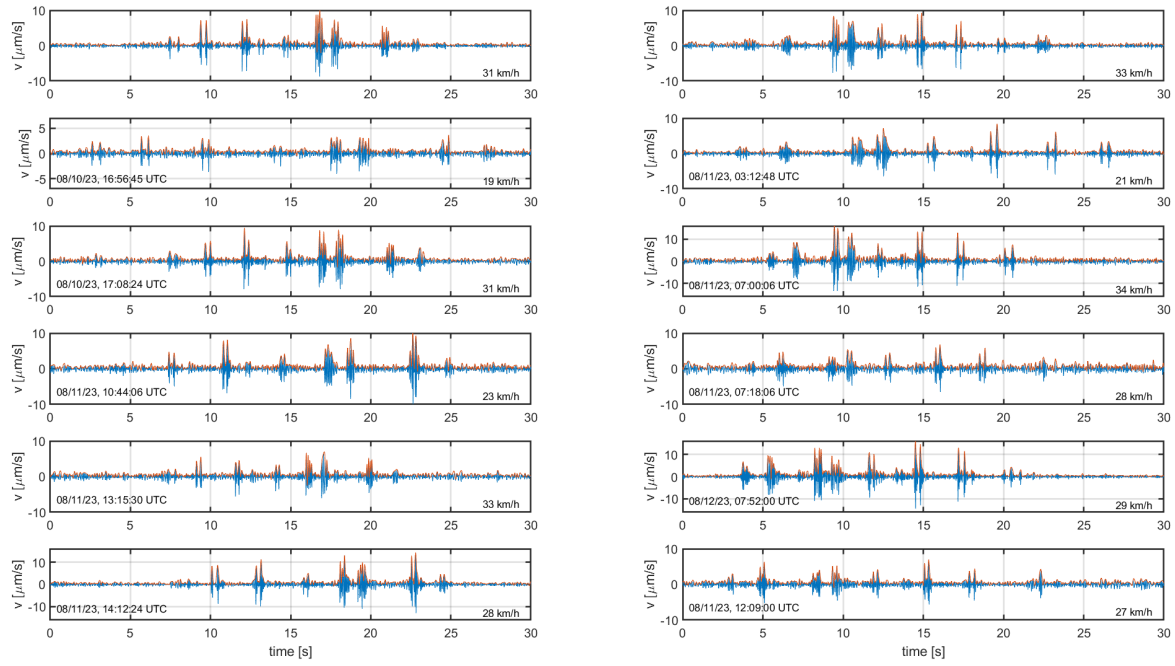

Supplemental Figure S11: Examples of signals from cars driving east to west (left column) or west to east (right column) past the array. Shown are vertical components filtered between 5 and 30 Hz in blue and their envelopes in orange. Start time of each window and the measured velocity along the whole track are listed. The topmost two signals are the ones shown in Fig. 6.

References

K. Aki. Space and time spectra of stationary stochastic waves, with special reference to microtremors. *Bulletin of the Earthquake Research Institute*, 35:415–456, 1957.

S. Bonnefoy-Claudet, C. Cornou, P.-Y. Bard, F. Cotton, P. Moczo, J. Kristek, and D. Fäh. H/V ratio: a tool for site effects evaluation. Results from 1-D noise simulations. *Geophysical Journal International*, 167(2):827–837, 2006. doi: 10.1111/j.1365-246X.2006.03154.x.

J. Capon. High-resolution frequency-wavenumber spectrum analysis. *Proceedings of the IEEE*, 57(8): 1408–1418, 1969. doi: 10.1109/PROC.1969.7278.

B. Endrun, M. Ohrnberger, and A. Savvaidis. On the repeatability and consistency of three-component ambient vibration array measurements. *Bulletin of Earthquake Engineering*, 8:535–570, 2010. doi: 10.1007/s10518-009-9159-9.

H.-H. Essen, F. Krüger, T. Dahm, and I. Grevemeyer. On the generation of secondary microseisms observed in northern and central europe. *Journal of Geophysical Research: Solid Earth*, 108(B10): 2506, 2003. doi: 10.1029/2002JB002338.

M. Hobiger, P.-Y. Bard, C. Cornou, and N. Le Bihan. Single station determination of Rayleigh wave ellipticity by using the random decrement technique (RayDec). *Geophysical Research Letters*, 36(14), 2009. doi: 10.1029/2009GL038863.

M. Hobiger, N. Le Bihan, C. Cornou, and P.-Y. Bard. Multicomponent signal processing for rayleigh wave ellipticity estimation: application to seismic hazard assessment. *IEEE Signal Processing Magazine*, 29 (3):29–39, 2012. doi: 10.1109/MSP.2012.2184969.

A. Köhler, M. Ohrnberger, F. Scherbaum, M. Wathelet, and C. Cornou. Assessing the reliability of the modified three-component spatial autocorrelation technique. *Geophysical Journal International*, 168 (2):779–796, 2007. doi: 10.1111/j.1365-246X.2006.03253.x.

K. Konno and T. Ohmachi. Ground-motion characteristics estimated from spectral ratio between horizontal and vertical components of microtremor. *Bulletin of the Seismological Society of America*, 88 (1):228–241, 1998. doi: 10.1785/BSSA0880010228.

R. T. Lacoss, E. J. Kelly, and M. N. Toksöz. Estimation of seismic noise structure using arrays. *Geophysics*, 34(1):21–38, 1969. doi: 10.1190/1.1439995.

S. Maranò, M. Hobiger, P. Bergamo, and D. Fäh. Analysis of Rayleigh waves with circular wavefront: a maximum likelihood approach. *Geophysical Journal International*, 210(3):1570–1580, 2017. doi: 10.1093/gji/ggx225.

Y. Nakamura. A method for dynamic characteristics estimation of subsurface using microtremor on the ground surface. *Railway Technical Research Institute, Quarterly Reports*, 30(1), 1989.

E. A. Olafsdottir, S. Erlingsson, and B. Bessason. Tool for analysis of multichannel analysis of surface waves (MASW) field data and evaluation of shear wave velocity profiles of soils. *Canadian Geotechnical Journal*, 55(2):217–233, 2018. doi: 10.1139/cgj-2016-0302.

S. Parolai, S. M. Richwalski, C. Milkereit, and P. Bormann. Assessment of the stability of H/V spectral ratios from ambient noise and comparison with earthquake data in the Cologne area (Germany). *Tectonophysics*, 390(1-4):57–73, 2004. doi: 10.1016/j.tecto.2004.03.02.

M. Pilz, C. Nievas, F. Cotton, K. Prehn, H. Razafindrakoto, D. Schorlemmer, G. Wetherill, T. Spies, and T. Lege. Seismic risk analysis in Germany: an example from the Lower Rhine Embayment. Final report. scientific technical report str 20/02, GFZ German Research Centre for Geosciences, Potsdam, 2020.

F. Robel. Die Erdbebenstation Bensberg bei Köln. *Zeitschrift für Geophysik*, pages 16–32, 1959.

K. Stammler, M. Bischoff, A. Brüstle, L. Ceranna, S. Donner, K. Fischer, P. Gaebler, W. Friederich, S. Funke, G. Hartmann, B. Homuth, B. Knapmeyer-Endrun, M. Korn, T. Megies, C. Pilger, T. Plenefisch, I. Pustal, I. Rappsilber, B. Schmidt, L. Sonnabend, S. Stange, J. Wassermann, and U. Wegler. German seismic and infrasound networks contributing to the European integrated data archive (EIDA). *Seismological Research Letters*, 92(3):1854–1875, 2021. doi: 10.1785/0220200401.

The ObsPy Development Team. ObsPy 1.4.0 (1.4.0), 2022.

S. Tyagunov, D. Hollnack, and F. Wenzel. Engineering-seismological analysis of site effects in the area of Cologne. *Natural Hazards*, 38:199–214, 2006. doi: 0.1007/s11069-005-8613-5.

Universität zu Köln. Im Jahr 2023 registrierte Lokalbeben an der Erdbebenstation Bensberg, 2023. URL `http://www.seismo.uni-koeln.de/catalog/2023.htm`. last accessed 2025/02/07.

M. Wathelet, B. Guillier, P. Roux, C. Cornou, and M. Ohrnberger. Rayleigh wave three-component beamforming: signed ellipticity assessment from high-resolution frequency-wavenumber processing of ambient vibration arrays. *Geophysical Journal International*, 215(1):507–523, 2018. doi: 10.1093/gji/ggy286.

M. Wathelet, J.-L. Chatelain, C. Cornou, G. D. Giulio, B. Guillier, M. Ohrnberger, and A. Savvaidis. Geopsy: A user-friendly open-source tool set for ambient vibration processing. *Seismological Research Letters*, 91(3):1878–1889, 2020. doi: 10.1785/0220190360.